Numerical calculation of three dimensional MHD natural convection based on spectral collocation method and artificial compressibility method

Jiapeng Chang[1], †*Jingkui Zhang[1,2], Qifen Li[1], Yi Fan[1], Jiakai Zhang[1]

[1]College of Energy and Mechanical Engineering, Shanghai University of Electric Power, Shanghai 200090, China.

[2]Shanghai Non-carbon energy conversion and utilization institute，Shanghai 200240, China.

*Presenting author: zk_neu@163.com

†Corresponding author: zk_neu@163.com

Abstract

The flow and heat transfer characteristics of a three-dimensional cavity filled with a conducting fluid are investigated in this study. The three-dimensional Navier-Stokes equations and energy equation are solved directly using our self-developed algorithm, SCM-ACM, which combines the spectral collocation method (SCM) with high-precision and exponential convergence, and the artificial compression method (ACM) with easy implementation and good numerical stability. In this paper, we examine the effects of Hartmann numbers (*Ha*) ranging from 0 to 100, magnetic field directions, and Grashof numbers (*Gr*) ranging from 1×10^4 to 1×10^6 on the structure of the flow and temperature fields, with a Prandtl number (*Pr*) of 0.71. The results show the Grashof and Hartmann number have a significant impact on the flow and temperature structure in the middle of the cube, but little effect on that near the walls. As the Grashof number increases, a stable thermal stratification is formed at the center of the cube, and thermal boundary layers are formed near the horizontal walls. The increase in Grashof number enhances the heat transfer rate and increases the temperature difference between the upper hot fluid and the lower cold fluid in the cube. Furthermore, the increase in Grashof number enhances the convective intensity between the isothermal walls, leading to the formation of more vortices, which move towards the corners due to the combined action of centrifugal force and inertia. The Hartmann number has a stabilizing effect on the flow and weakens the heat transfer, while at higher Grashof numbers, the magnetic effect becomes more notable. When $Ha>50$, the magnetic effect is no longer significant. The magnetic field parallel to the temperature gradient (B_X) is more effective in suppressing heat transfer than the magnetic field perpendicular to the temperature gradient (B_Y). The methods and conclusions have certain theoretical guidance for the design and optimization of relevant engineering fields.

Keywords: Spectral collocation method, artificial compression method, magnetohydrodynamics, three-dimensional natural convection

Introduction

Natural convection flow is one of the important phenomenon in fluid mechanics, which has been widely observed in natural systems and engineering applications[1]–[4]. The control of the flow direction and heat transfer rate of conducting fluids by an externally applied magnetic field has attracted significant attention in the fields of thermodynamics and fluid mechanics. Consequently, magnetohydrodynamics (MHD) has experienced substantial development and application in the past decade[5], [6]. In this study, a three-dimensional cavity filled with a conductive fluid is investigated to examine the effects of the applied magnetic field intensity, Grashof number, and magnetic field orientation on the heat transfer rate and flow structure.

Natural convection heat transfer inside an enclosure is a fundamental heat transfer mechanism[7]. The heat boundary conditions, fluid properties, and intensity and directions of the magnetic field all have significant effects on the flow structure. The initial research focused on two-dimensional models. Bondareva et al. [8] studied the natural convective phase transformation process of solid pure potassium in a cavity with an internal heat source under the action of an inclined magnetic field. They concluded that the average Nusselt number (Nu_{avg}) increased with the tilt angle of the magnetic field and decreased with the Hartmann number. Saleh et al. [9] used the finite difference method to study the heat transfer in a rotating cavity under a magnetic field. They analyzed the effects of the strength and directions of the magnetic field and the rotation speed of the square cavity on heat transfer. Rudraiah et al. [10] found that when the magnetic field was relatively strong, the fluid in most areas of the shell almost stagnated. Sivasankaran et al. [11] used the finite volume method to study the influence of temperature-related characteristics of water near the density extremum on fluid flow and heat transfer under a uniform magnetic field. They found that the heat transfer rate increased with the increase of Rayleigh number (*Ra*) and decreased with the increase of Hartmann number.

In recent years, some scholars have conducted research on natural convection of magnetohydrodynamics in a three-dimensional cavity, benefiting from the optimization of numerical methods and the improvement of computational power. Sajjadi et al. [12], [13] studied the effects of Rayleigh number and magnetic field strength on heat transfer using the lattice Boltzmann method. They found that increasing the Rayleigh number enhances the heat transfer rate, while increasing the Hartmann number had the opposite effect. Later, Zhou et al. [14] used the same method to investigated the flow dynamics and mixed heat transfer of an Al_2O_3/water nanofluid in a cubic cavity. Their results showed that the Richardson number (*Ri*) has a significant impact on both the flow and temperature fields. Ellahi et al. [15] studied the heat transfer in a cavity with a pair of adiabatic horizontal and spanwise walls. They concluded that the Nusselt number (*Nu*) increases with the Rayleigh number. Zikanov et al. [16] investigated the effects of the magnetic field orientation on natural convection heat transfer using the finite volume method. Their results showed that the magnetic field parallel to the temperature gradient could maximally suppress heat transfer. Bouchta et al. [17] studied the heat transfer behavior of a particle-fluid mixture in a cavity with adiabatic horizontal and spanwise walls using the finite volume method and analyzed the relative positions of hot and cold walls on heat transfer. Okada et al. [18], [19] investigated the effects of different magnetic field directions and strengths using experimental and numerical simulation methods. They found that the magnetic field parallel to the temperature gradient could suppress the heat transfer rate by a factor of 10 compared to the horizontal magnetic field perpendicular to the temperature gradient.

Currently, most studies on MHD flow utilize finite element method, finite difference method, or lattice Boltzmann method. Traditional spatial discretization schemes require high spatial and temporal accuracy to directly solve the governing equations of natural convection in MHD, leading to significantly increased computational costs especially with lager Grashof number. The SCM exhibits exponential convergence and high accuracy. Therefore, employing this method for spatial discretization can achieve higher accuracy while computational costs can be greatly reduced. Additionally, the ACM possesses advantages such as numerical stability and easy convergence. Hence, in this study, we directly solve the MHD natural convection equations using the SCM-ACM. Regarding the research scope,

numerous studies assume that the horizontal and spanwise walls of the cavity are adiabatic. However, achieving such ideal thermal boundary conditions in experiments and practical engineering applications is challenging. Considering the numerical solutions as theoretical guidance for real-world engineering applications, we introduce a cubic cavity with one pair of isothermal walls, while the remaining four walls are conductive. We conducted a detailed investigation on the effect of magnetic field intensity, Grashof numbers, and magnetic field directions on the three-dimensional flow and heat transfer.

2. Mathematical Description

In this work, the natural convection flow characteristics of MHD are analyzed in a three-dimensional cavity. As shown in Fig. 1, the cavity with edge length L (L=1) is filled with viscous, incompressible, and electrically conductive fluid. The vertical walls (X=0 and X=L) are maintained at constant temperatures of T_h and T_c (T_h>T_c), respectively, while the other four walls are assumed to be perfectly conductive. The magnetic field is applied parallel to the coordinate axes, such as the magnetic field B_X in the X direction.

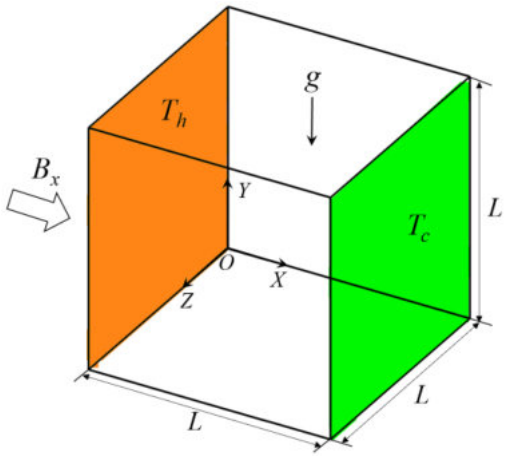

Fig. 1. The geometric model for the natural convection.

Since the Hartmann number (0-100) is not very large and the magnetic Reynolds number Re_m<<1, the induce magnetic field can be ignored. The ACM method adds $\partial p/\partial t$, $\partial \boldsymbol{u}/\partial t$ and $\partial T/\partial t$ to the continuity, momentum, and energy equations, respectively. When the solution time is long enough, the steady-state results can be obtained [20]. ACM is widely used due to its simplicity and ease of convergence when solving incompressible or weakly compressible flow equations [21]–[24].

$$\frac{\partial p}{\partial t} + c^2 \nabla \cdot \boldsymbol{u} = 0 \tag{1}$$

$$\frac{D\boldsymbol{u}}{Dt} = -\nabla\left(\frac{p}{\rho}\right) + \nabla \cdot (v\nabla \boldsymbol{u}) + \frac{1}{\rho}\boldsymbol{J} \times \boldsymbol{B} \tag{2}$$

$$\frac{\partial T}{\partial t} + \nabla \cdot (\boldsymbol{u}T) = \alpha \nabla^2 T \tag{3}$$

where p, $\boldsymbol{u}$, ρ, v, T, α and t are the pressure, velocity vector, density, kinematic viscosity, temperature, thermal diffusivity and the pseudo time, respectively. c is the artificial compressibility parameter. For all the cases in this paper, c=1.5 [25]. $\boldsymbol{J}$ is the current density, $\boldsymbol{J}=\varepsilon(\boldsymbol{u}\times\boldsymbol{B})$, where ε and $\boldsymbol{B}$ are the conductivity and magnetic field.

In order to make the obtained results universal, each variable is dimensionless through Eq. (4).

$$X=\frac{x}{L},Y=\frac{y}{L},Z=\frac{z}{L},U=\frac{u}{U_0},V=\frac{v}{U_0},W=\frac{w}{U_0},P=\frac{p}{\rho U_0^2},\theta=\frac{T}{T_r} \tag{4}$$

where x, y and z are the Cartesian coordinates. X, Y and Z are the dimensionless Cartesian coordinates, respectively. U, V and W are the dimensionless velocities in X-, Y- and Z-directions. L and U_0 are the reference length and the reference velocity. P is the dimensionless pressure. θ and T_r are the dimensionless temperature and reference temperature. The ACM equations for three-dimensional natural convection in dimensionless form are as follows.

$$\frac{\partial P}{\partial t}+c^2\left(\frac{\partial U}{\partial X}+\frac{\partial V}{\partial Y}+\frac{\partial W}{\partial Z}\right)=0 \tag{5}$$

$$\frac{\partial U}{\partial t}+\frac{\partial}{\partial X}(U^2)+\frac{\partial}{\partial Y}(VU)+\frac{\partial}{\partial Z}(WU)=-\frac{\partial P}{\partial X}+\frac{1}{Re}\nabla^2U+F_x \tag{6}$$

$$\frac{\partial V}{\partial t}+\frac{\partial}{\partial X}(UV)+\frac{\partial}{\partial Y}(V^2)+\frac{\partial}{\partial Z}(WV)=-\frac{\partial P}{\partial Y}+\frac{1}{Re}\nabla^2V+F_y \tag{7}$$

$$\frac{\partial W}{\partial t}+\frac{\partial}{\partial X}(UW)+\frac{\partial}{\partial Y}(VW)+\frac{\partial}{\partial Z}(W^2)=-\frac{\partial P}{\partial Z}+\frac{1}{Re}\nabla^2W+F_z \tag{8}$$

$$\frac{\partial \theta}{\partial t}+\frac{\partial}{\partial X}(U\theta)+\frac{\partial}{\partial Y}(V\theta)+\frac{\partial}{\partial Z}(W\theta)=\frac{1}{PrRe}\nabla^2\theta \tag{9}$$

where Re is the Reynold number, $Re=\frac{U_0L}{v}$,. Pr is the Prandtl number, $Pr=v/\alpha$. F_x, F_y and F_z are the source terms in X-, Y- and Z-directions. Taking the magnetic field along the Y direction as an example, there are $F_x=\frac{Ha^2}{Re}U$, $F_y=\frac{Ra}{PrRe^2}\theta$ and $F_z=\frac{Ha^2}{Re}W$. Ra is the Rayleigh number, $Ra=\frac{g\beta(T_h-T_c)L^3}{\alpha v}$, where β is the thermal expansion coefficient and g is the gravitational acceleration. Ha is the Hartmann number, $Ha=B_yL\sqrt{\frac{\varepsilon}{\mu}}$, where μ is the dynamic viscosity.

All walls are assumed to be non-slip. The two vertical walls located at X=0 and X=1 are assumed to be isothermal.

$$\theta|_{X=0}=1,\ \theta|_{X=1}=0 \tag{10}$$

Both horizontal and spanwise walls conduct heat.

$$\theta|_{Y=0,\,1}=\theta|_{Z=0,\,1}=1-X \tag{11}$$

The rate of heat transfer is characterized by the local Nusselt number (Nu_{local}) and the average Nusselt number, which can be obtained based on the temperature field.

$$Nu_{local}=\left.\frac{-L}{\Delta T}\frac{\partial T}{\partial x}\right|_{x=0,L} \tag{12}$$

$$Nu_{\text{avg}}=\frac{1}{A}\int_A Nu_{lacal}dA=\frac{1}{A}\iint Nu_{local}dydz \tag{13}$$

3. Numerical method

3.1 Spectral collocation method

Spectral methods are widely used to solve problems related to flow, heat, and mass transfer due to their high accuracy and exponential convergence [26]–[29]. In this paper, Chebyshev-Gauss-Lobatto (CGL) collocation point pairs are chosen to discretize equations (5)-(9) spatially. Here, the X direction is considered for illustration. The first step involves selecting the configuration points. The location r_i of CGL collocation point N can be determined as follows.

$$r_i = -\cos\frac{\pi i}{N},\ i = 0,\cdots,N \tag{14}$$

where r_i is the location of CGL collocation point i in X coordinate. N is the CGL collocation points in X coordinate.

The second step is to transform the computational domain. Eq. (15) is used to convert the actual physical interval $\{\mathbf{E}:(X)\in[X_{\min},\ X_{\max}]\}$ into a standard spectral interval $\{\mathbf{E}:(r)\in[-1,\ 1]\}$. The spatial partial derivatives after the transformation are as follows.

$$r = \frac{2X-(X_{\max}+X_{\min})}{X_{\max}-X_{\min}},\ r\in[-1,\ 1] \tag{15}$$

$$\begin{cases}\dfrac{\partial\phi}{\partial X} = \dfrac{\partial\phi}{\partial r}\dfrac{\partial r}{\partial X} = \dfrac{2}{(X_{\max}-X_{\min})}\dfrac{\partial\phi}{\partial r}\\[2ex] \dfrac{\partial^2\phi}{\partial X^2} = \left(\dfrac{2}{X_{\max}-X_{\min}}\right)^2\dfrac{\partial^2\phi}{\partial r^2}\end{cases} \tag{16}$$

Thirdly, the spatial partial derivatives are replaced by truncated series. The general variable $\phi(r)$ can be approximated on collocation points by truncated series as:

$$\phi(r)\approx\sum_{j=0}^{N}\phi(r_j)h_j(r) \tag{17}$$

where $h_j(r)$ is the Lagrange interpolation polynomial, and the expression is given as follows.

$$h_j(r) = \frac{(-1)^{j+1}(1-r^2)T_N'(r)}{c_jN^2(r-r_j)} \tag{18}$$

$$c_j = \begin{cases}2,\ j=0,N\\ 1,\ j=1,\cdots,N-1\end{cases} \tag{19}$$

where $T_N'(r)$ is the first-order derivative of the Chebyshev polynomial $T_N(r)$.

$$T_N(r) = \cos\left(i\cos^{-1}(r)\right),\ i=0,\cdots,N \tag{20}$$

So, the expressions of the first-order and second-order derivatives at $r=r_0$ are as follows.

$$\frac{\partial\phi(r)}{\partial r}\Big|_{r=r_0} = \sum_{j=0}^{N}h_j^{(1)}(r_0)\phi(r_j) = \sum_{j=0}^{N}\boldsymbol{D}_{ij}^{(1)}\phi(r_j),\ i=0,\cdots,N \tag{21}$$

$$\frac{\partial^2\phi(r)}{\partial r^2}\Big|_{r=r_0} = \sum_{j=0}^{N}h_j^{(2)}(r_0)\phi(r_j) = \sum_{j=0}^{N}\boldsymbol{D}_{ij}^{(2)}\phi(r_j),\ i=0,\cdots,N \tag{22}$$

where $h^{(1)}$ and $h^{(2)}$ are the first-order and second-order derivatives of $h(r)$. $\boldsymbol{D}^{(1)}$ and $\boldsymbol{D}^{(2)}$ are the first-order and second-order coefficient matrices corresponding to the CGL collocation points. The elements of coefficient matrices are shown as follows.

$$\boldsymbol{D}_{ij}^{(1)}=\begin{cases}\dfrac{c_i(-1)^{i+j}}{c_j(r_i-r_j)}, & i\neq j\\ \dfrac{-r_j}{2\left(1-r_j^{\,2}\right)}, & 1\le i=j\le N-1\\ \dfrac{2N^2+1}{6}, & i=j=0\\ -\dfrac{2N^2+1}{6}, & i=j=N\end{cases},\quad \boldsymbol{D}_{ij}^{(2)}=\begin{cases}\dfrac{(-1)^{i+j}\left(r_i^2+r_ir_j-2\right)}{c_j\left(1-r_i^2\right)\left(r_i-r_j\right)^2}, & 1\le i\le N-1,\ 0\le j\le N,\ i\neq j\\ -\dfrac{\left(N^2-1\right)\left(1-r_i^2\right)+3}{3\left(1-r_i^2\right)^2}, & 1\le i=j\le N-1\\ \dfrac{2(-1)^j\left(2N^2+1\right)\left(1-r_j\right)-6}{3c_j\left(1-r_j\right)^2}, & i=0,\ 1\le j\le N\\ \dfrac{2(-1)^{(j+N)}\left(2N^2+1\right)\left(1-r_j\right)-6}{3c_j\left(1+r_j\right)^2}, & i=N,\ 1\le j\le N-1\\ \dfrac{N^4-1}{15}, & i=j=0,N\end{cases} \tag{23}$$

Therefore, the dimensionless governing equations (5)-(9) can be discretized in space as follows.

$$\frac{\partial P}{\partial t}+c^2\left(\sum_{l=0}^{N_x}\boldsymbol{A}_{il}U_{ljk}+\sum_{l=0}^{N_y}\boldsymbol{B}_{jl}V_{ilk}+\sum_{l=0}^{N_z}\boldsymbol{C}_{kl}W_{ijl}\right)=0 \tag{24}$$

$$\begin{aligned}&\frac{\partial U}{\partial t}+U_{ijk}\sum_{l=0}^{N_x}\boldsymbol{A}_{il}U_{ljk}+V_{ijk}\sum_{l=0}^{N_y}\boldsymbol{B}_{jl}U_{ilk}+W_{ijk}\sum_{l=0}^{N_z}\boldsymbol{C}_{kl}U_{ijl}=\\ &-\sum_{l=0}^{N_x}\boldsymbol{A}_{il}P_{ljk}+\frac{1}{Re}\left(\sum_{l=0}^{N_x}\boldsymbol{E}_{il}U_{ljk}+\sum_{l=0}^{N_y}\boldsymbol{F}_{jl}U_{ilk}+\sum_{l=0}^{N_z}\boldsymbol{M}_{kl}U_{ijl}\right)\end{aligned} \tag{25}$$

$$\begin{aligned}&\frac{\partial V}{\partial t}+U_{ijk}\sum_{l=0}^{N_x}\boldsymbol{A}_{il}V_{ljk}+V_{ijk}\sum_{l=0}^{N_y}\boldsymbol{B}_{jl}V_{ilk}+W_{ijk}\sum_{l=0}^{N_z}\boldsymbol{C}_{kl}V_{ijl}=\\ &-\sum_{l=0}^{N_y}\boldsymbol{B}_{jl}P_{ilk}+\frac{1}{Re}\left(\sum_{l=0}^{N_x}\boldsymbol{E}_{il}V_{ljk}+\sum_{l=0}^{N_y}\boldsymbol{F}_{jl}V_{ilk}+\sum_{l=0}^{N_z}\boldsymbol{M}_{kl}V_{ijl}\right)+\frac{Gr}{Re^2}\theta-\frac{Ha^2}{Re}V_{ijk}\end{aligned} \tag{26}$$

$$\begin{aligned}&\frac{\partial W}{\partial t}+U_{ijk}\sum_{l=0}^{N_x}\boldsymbol{A}_{il}W_{ljk}+V_{ijk}\sum_{l=0}^{N_y}\boldsymbol{B}_{jl}W_{ilk}+W_{ijk}\sum_{l=0}^{N_z}\boldsymbol{C}_{kl}W_{ijl}=\\ &-\sum_{l=0}^{N_z}\boldsymbol{C}_{kl}P_{ijl}+\frac{1}{Re}\left(\sum_{l=0}^{N_x}\boldsymbol{E}_{il}W_{ljk}+\sum_{l=0}^{N_y}\boldsymbol{F}_{jl}W_{ilk}+\sum_{l=0}^{N_z}\boldsymbol{M}_{kl}W_{ijl}\right)-\frac{Ha^2}{Re}W_{ijk}\end{aligned} \tag{27}$$

$$\frac{\partial\theta}{\partial t}+U_{ijk}\sum_{l=0}^{N_x}\boldsymbol{A}_{il}\theta_{ljk}+V_{ijk}\sum_{l=0}^{N_y}\boldsymbol{B}_{jl}\theta_{ilk}+W_{ijk}\boldsymbol{C}_{kl}\theta_{ijl}=\frac{1}{RePr}\left(\sum_{l=0}^{N_x}\boldsymbol{E}_{il}\theta_{ljk}+\sum_{l=0}^{N_y}\boldsymbol{F}_{il}\theta_{ilk}+\sum_{l=0}^{Nz}\boldsymbol{M}_{il}\theta_{ijl}\right) \tag{28}$$

where $\boldsymbol{A}$, $\boldsymbol{B}$ and $\boldsymbol{C}$ are the first-order coefficient matrix $\boldsymbol{D}^{(1)}$ for configuration points N_x, N_y, and N_z corresponding to directions *X*-, *Y*-, and *Z*-directions, while $\boldsymbol{E}$, $\boldsymbol{F}$ and $\boldsymbol{M}$ are the second-order coefficient matrices $\boldsymbol{D}^{(2)}$ for configuration points corresponding to directions *X*-, *Y*-, and *Z*-directions.

The explicit fourth-order Runge-Kutta scheme is adopted in this paper for the discretization of the time term [20], [25], which is known for its excellent performance in solving incompressible fluid flows.

To ensure obtaining the steady-state results using ACM, it is necessary to solve for a sufficiently long time to make the unsteady term tend to 0. The calculation can be stopped when the maximum residuals of all variables at two adjacent time steps satisfy Eq. (29), where ε is the tolerance and is set as $\varepsilon = \Delta t \times 10^{-4}$.

$$\max\left(\left|U^{n+1}-U^{n}\right|,\ \left|V^{n+1}-V^{n}\right|,\ \left|W^{n+1}-W^{n}\right|,\ \frac{1}{c^2}\left|P^{n+1}-P^{n}\right|,\ \left|\theta^{n+1}-\theta^{n}\right|\right)<\varepsilon \quad (29)$$

3.2 Grid independence test

We employ four sets of grid nodes as 22×22×22, 32×32×32, 42×42×42, and 52×52×52, to investigate grid test. For the selected case (Ha_Y=10, Gr=1×10^5, and Pr=0.71), after attaining convergence of the iterative results, we compare the average Nusselt numbers on the cold wall under different grid schemes. As depicted in Fig. 2, a significant variation in the average Nusselt numbers is observed when the number of nodes increases from 22^3 to 42^3. However, the average Nusselt number only changes by 0.055% when the number of nodes increases from 42^3 to 52^3. Taking the computational efficiency and accuracy into account, we select the 42^3-node configuration for spatial discretization.

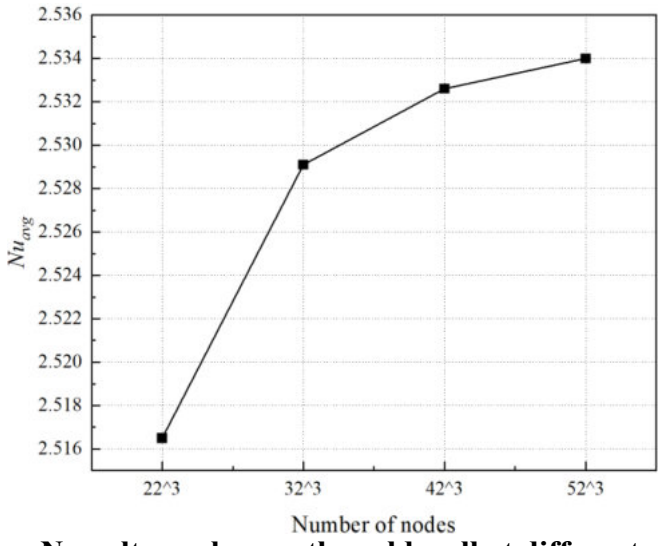

Fig. 2 The average Nusselt number on the cold wall at different number of nodes.

3.3 Code validation

The code validation is divided into two parts. First, the natural convection is verified without considering the magnetic field. We set the same thermal boundary conditions as those by Fusegi et al. [30], Tric et al. [31], Saitoh et al. [32], and Luo et al. [33]. Table 1 shows the calculated average Nusselt number of the hot wall, and our results exhibit good agreement with the existing results.

Table 1 The average Nusselt number on the hot wall of natural convection in a three-dimensional cavity with different *Ra* for *Pr*=0.71.

Ra	Fusegi et al.	Tric et al.	Saitoh et al.	Luo et al.	Present results
10^4	2.100	2.054	2.0624	2.057	2.0582
10^5	4.361	4.337	4.3665	4.337	4.3423
10^6	8.770	8.641	8.6973	8.648	8.6547

Next, we compare our results with those by Singh et al. [34] with the magnetic field condition, and Fig. 2 shows excellent agreement between our results and those in the literature.

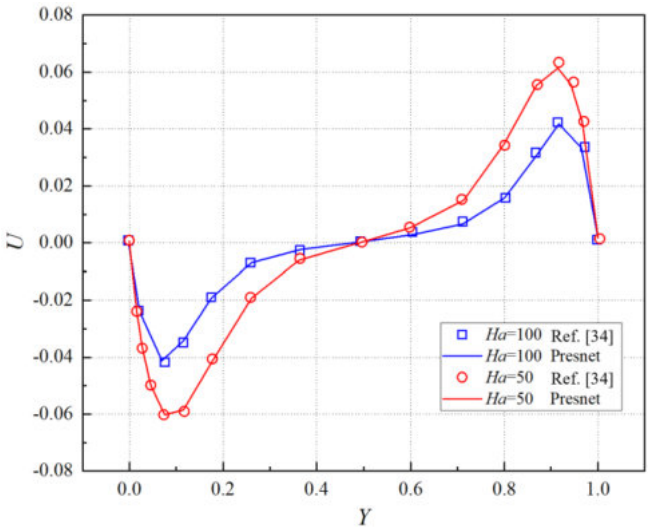

Fig. 3. The distribution of velocity (*U*) alone the line (0.5, *Y*, 0.5) for *Ha*=50 and 100.

4. Results and discussion

In this study, the SCM-ACM numerical method is employed to solve the natural convection of MHD in a three-dimensional cavity with two isothermal walls and the remaining four walls being linear temperature distribution. The effects of Grashof numbers, magnetic field intensity and directions on flow and heat transfer are comprehensively analyzed through the examination of streamlines, isotherms and heat transfer rates.

4.1 Effects of Grashof number on natural convection

We firstly analyze the three-dimensional temperature isosurfaces. Fig. 4 shows that temperature isosurfaces gradually become curved with the increase of Grashof number. When $Gr=1\times10^6$, the isothermal surfaces become approximately parallel to the horizontal walls near the center of the cubic cavity, with little change near the vertical walls.

Then, the flow field and temperature field on the plane Z=0.5, Y=0.5 and X=0.5 are analyzed. Fig. 5 shows the isotherms on the main circulation surface (Z=0.5), where it is observed that the increase in Grashof number results in temperature stratification at the center of the cubic cavity. This leads to an increase in temperature gradient along the height direction, and subsequently, an increase in heat transfer rate. Moreover, as the Grashof number increases, the boundary layers near the two isothermal walls become thinner, and convective heat transfer has become the dominant mode of heat transfer. Since the horizontal surfaces are all thermally conductive, the boundary layers here develop faster.

Since the flow field and temperature field are coupled together, Fig. 6 shows that the streamlines at plane Z=0.5 also changes greatly. When the Grashof number (Gr=1×10^4) is relatively small, the natural convection is not strong enough to form more than one primary vortex. With the increase in the Grashof number to 1×10^5, the natural convection strengthens, and the number of vortices increases to two. When the Grashof number further increases to 1×10^6, the two vortices move towards the corners under the driving force of natural convection and eventually settle in the top-left and bottom-right corners. This is because the corners are the convergence points of the heat convection, providing enough space and conditions for the vortices to stay. In contrast, the center area is the divergence point of the heat convection, and the streamlines will spread out, making it unfavorable for the vortices to exist. The inertia force that causes the vortex to move towards the center and the centrifugal force that causes the vortex to move towards the corners reach a balance, resulting in the vortexes concentrating in the left upper and right lower corners.

Fig. 7 shows that at the plane Y=0.5 the increase in Grashof number makes the isotherms approaching the isothermal surfaces (X=0 and X=1), and the boundary layers of the isothermal surfaces become thinner, leading to an increase in heat transfer rate.

According to the streamlines at the plane Y=0.5 in Fig. 8, it can be observed that the number of streamline intersection points increases from two to four when the Grashof number increases from 1×10^4 to 1×10^5. Further increasing the Grashof number to 1×10^6, the flow intensity inside the cube continues to increase, and the four streamline intersection points gradually move to the four corners. This phenomenon occurs because the vortex structure can be better maintained in the corners of the cube, where there exists a stable pressure difference that makes it easier for the flow to form vortices.

Fig. 9 shows that in the cube, the hot fluid is located in the upper part, while the cold fluid is in the lower part. The phenomenon is caused by a combination of temperature gradients and gravity. As the Grashof number increases from 1×10^4 to 1×10^6, the convective strength increases, causing the upper part temperature to rise from 0.63 to 0.69 and the lower part temperature to decrease from 0.37 to 0.29. In other words, the temperature difference between the upper and lower parts of the cube becomes greater. This is because at higher Grashof numbers, the momentum and heat transfer become more intense, leading to more intense fluid motion and temperature distribution changes. The streamline in Fig. 10 changes greatly with the increase of Grashof number.

Fig. 11 demonstrates the effects of the Grashof number and Hartman number on heat transfer. The average Nusselt number on the hot wall increases with the Grashof number, and a larger Hartman number has a greater impact on the average Nusselt number. The average Nusselt number increases by 326.6 % when the Grashof number increases from 10^4 to 10^6 at Ha=0, while the increase is only 104.8 % at Ha=100.

Fig. 12 shows that the local Nusselt number increases with Grashof number and decreases with Hartman number. However, the position corresponding to the maximum value of local Nusselt number is not affected by changes in Hartman number and Grashof number. It should be noted that under strong magnetic fields (i.e., Ha=50 and 100), Fig. 12 (c) and Fig. 12 (d) show that the local Nusselt number decreases with increasing Grashof number at a height of 0.6-1.0 on the hot wall. This phenomenon is attributed to the fact that as the Grashof number increases, the effects of natural convection become more significant. While, the influence of the magnetic field also becomes stronger.

Fig. 13 illustrates that the velocity V distribution along the X direction is consistent under various Grashof numbers. Initially, the velocity is zero due to the no-slip boundaries. Subsequently, the velocity increases and reaches its maximum as a result of upward flow along the hot wall. Finally, the velocity decreases, and at the center of the cavity (X=0.5), the velocity is zero. The magnitudes of velocities in the left and right halves of the cubic cavity are equal but opposite in direction. Under the same Hartman number, as the Grashof number increases, the velocity near the wall increases while the velocity in the middle region of the cubic cavity decreases. For Ha=10, the maximum velocity corresponding to Gr=1×10^6 is approximately 1.6 times that of Gr=1×10^4. This value can reach 7.5 and 10.5 for Ha=50 and 100, respectively. Therefore, we conclude that the velocity difference under different Grashof numbers becomes more pronounced with an increase in Hartman number.

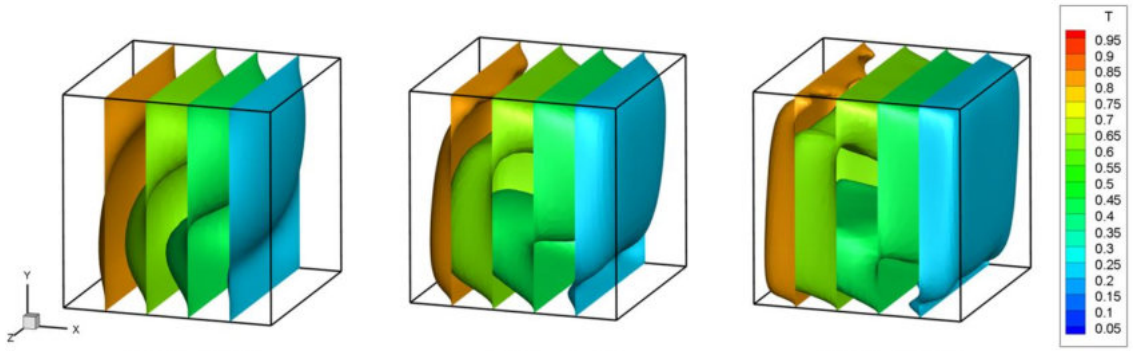

(a) Gr=1×10^4 (b) Gr=1×10^5 (c) Gr=1×10^6

Fig. 4. The distribution of three-dimensional temperature isosurfaces for (a) Gr= 1×10^4, (b) Gr=1×10^5, (c) Gr=1×10^6.

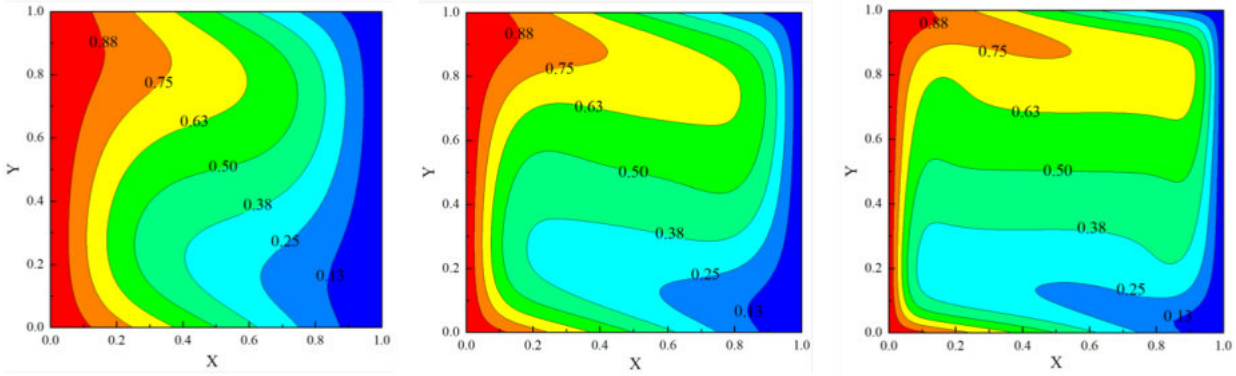

(a) Gr=1×10^4 (b) Gr=1×10^5 (c) Gr=1×10^6

Fig. 5. The distribution of temperature on the plane Z=0.5 for (a) Gr=1×10^4, (b) Gr=1×10^5 and (c) Gr=1×10^6.

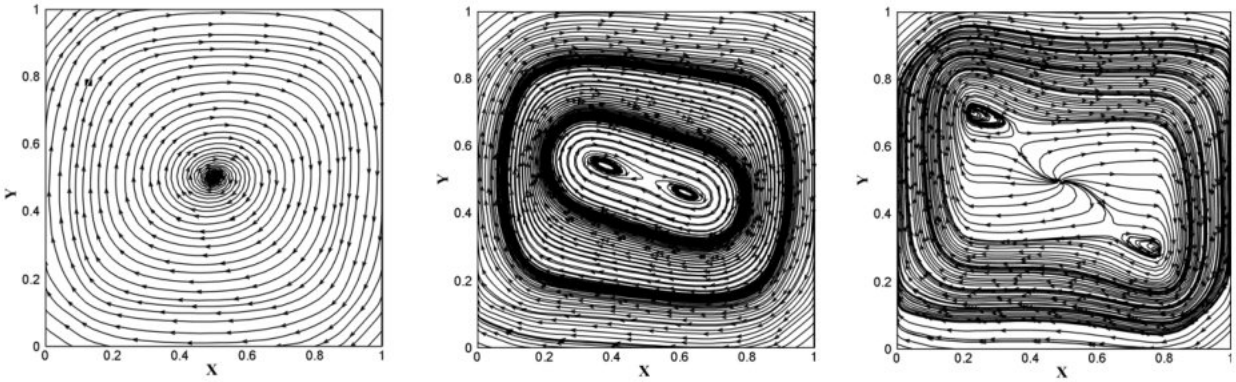

(a) Gr=1×10^4 (b) Gr=1×10^5 (c) Gr=1×10^6

Fig. 6. The distribution of streamline on the plane Z=0.5 for (a) Gr=1×10^4, (b) Gr=1×10^5 and (c) Gr=1×10^6.

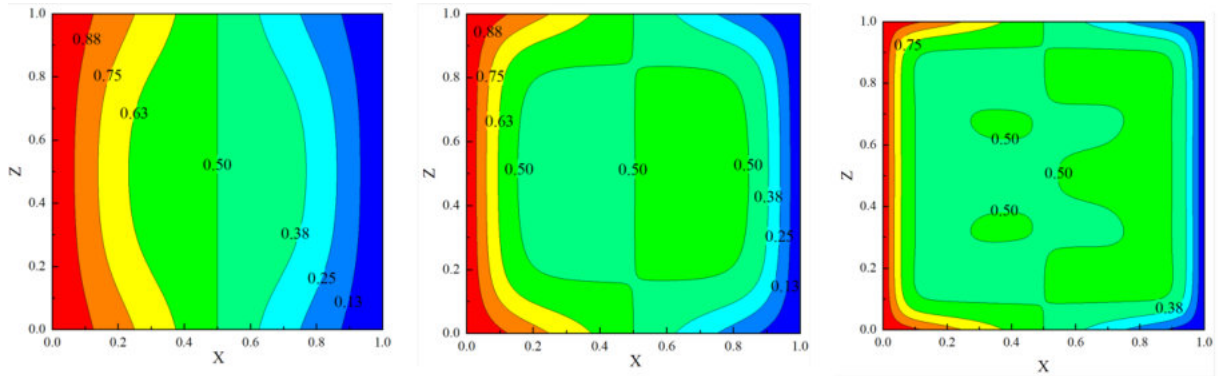

(a) Gr=1×10^4 (b) Gr=1×10^5 (c) Gr=1×10^6

Fig. 7. The distribution of temperature on the plane Y=0.5 for (a) Gr=1×10^4, (b) Gr=1×10^5 and (c) Gr=1×10^6.

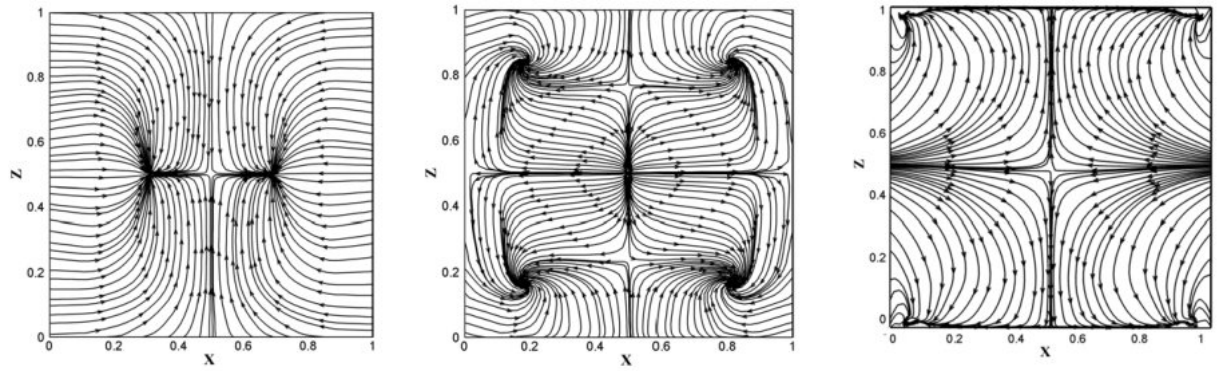

(a) Gr=1×10^4 (b) Gr=1×10^5 (c) Gr=1×10^6

Fig. 8. The distribution of streamline on the plane Y=0.5 for (a) Gr=1×10^4, (b) Gr=1×10^5 and (c) Gr=1×10^6.

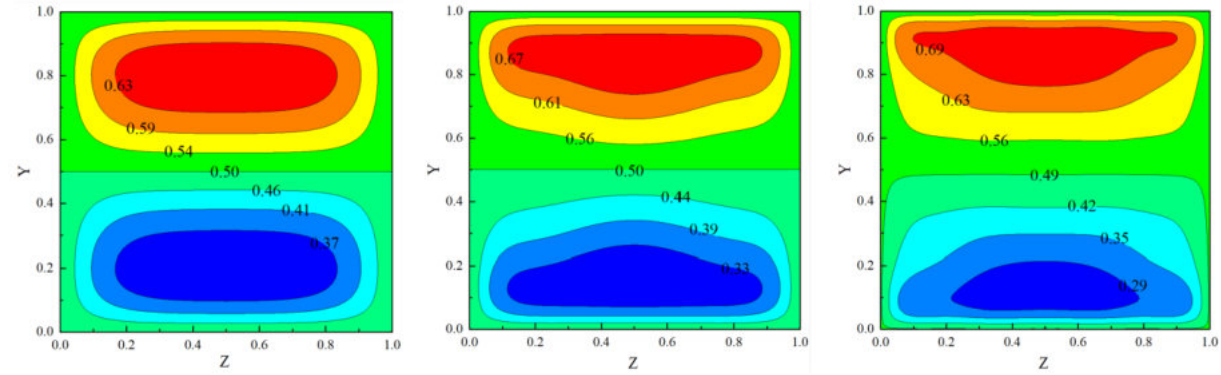

(a) Gr=1×10^4 (b) Gr=1×10^5 (c) Gr=1×10^6

Fig. 9. The distribution of temperature on the plane X=0.5 for (a) Gr=1×10^4, (b) Gr=1×10^5 and (c) Gr=1×10^6.

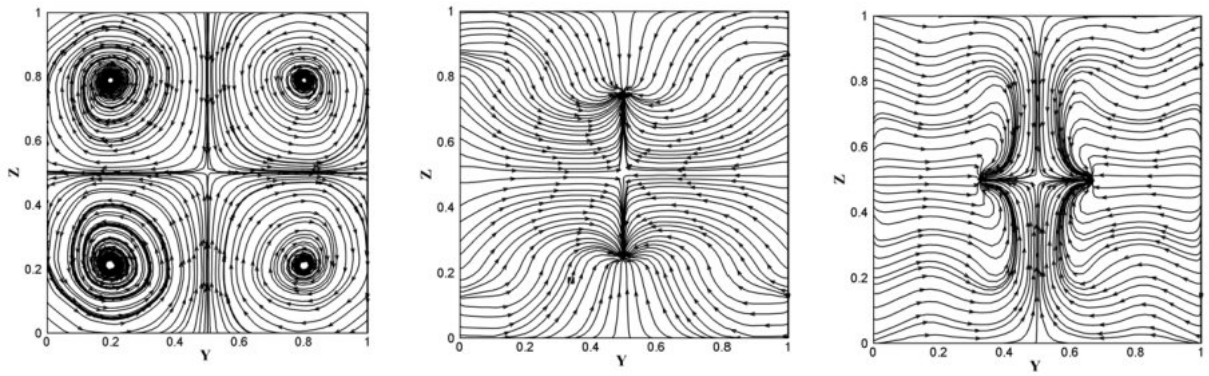

(a) Gr=1×10^4 (b) Gr=1×10^5 (c) Gr=1×10^6

Fig. 10. The distribution of streamline on the plane X=0.5 for (a) Gr=1×10^4, (b) Gr=1×10^5 and (c) Gr=1×10^6.

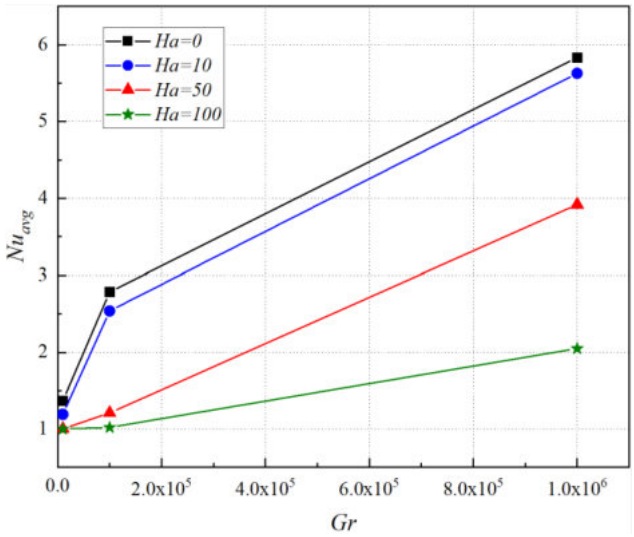

Fig. 11 The distribution of average Nusselt number with Grashof numbers on the hot wall for different Hartman numbers.

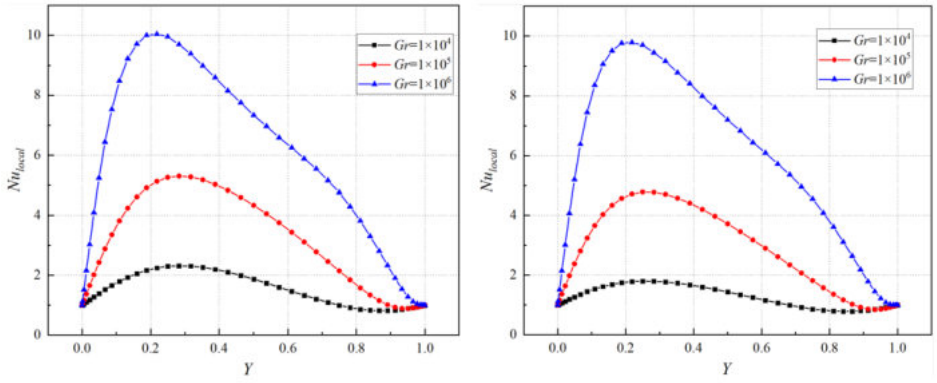

(a) Ha=0 (b) Ha=10

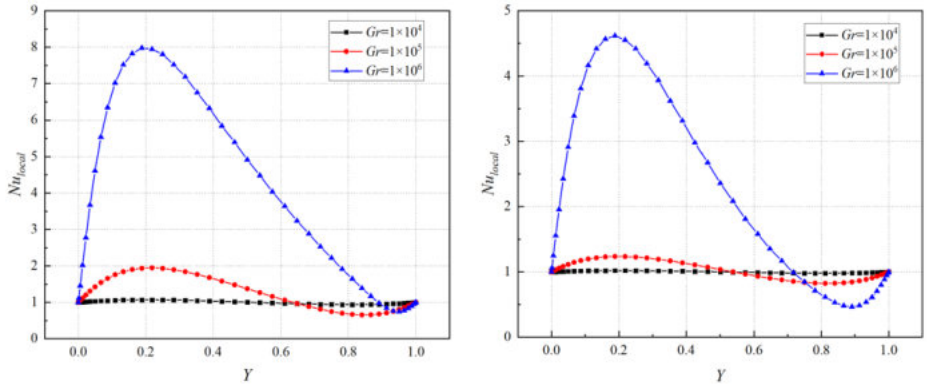

(c) *Ha*=50 (c) *Ha*=100

Fig. 12. The distribution of local Nusselt number alone the line (0, *Y*, 0.5) for (a) *Ha*=0, (b) *Ha*=10, (c) *Ha*=50 and (d) *Ha*=100.

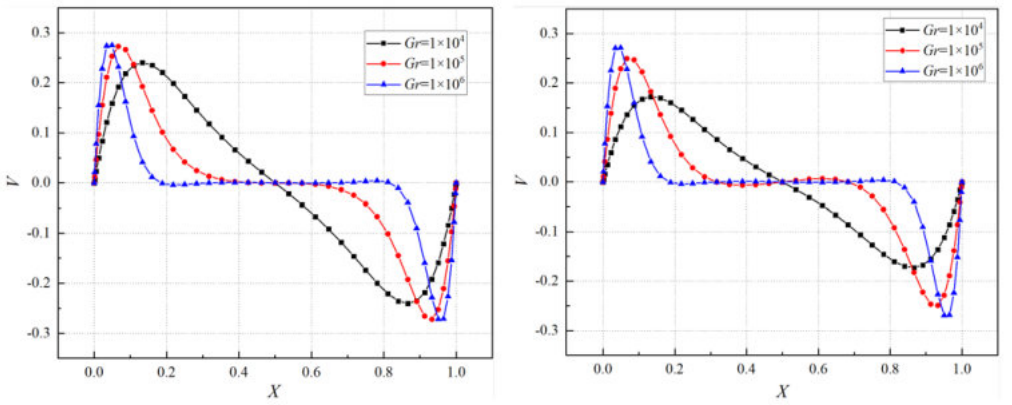

(a) *Ha*=0 (b) *Ha*=10

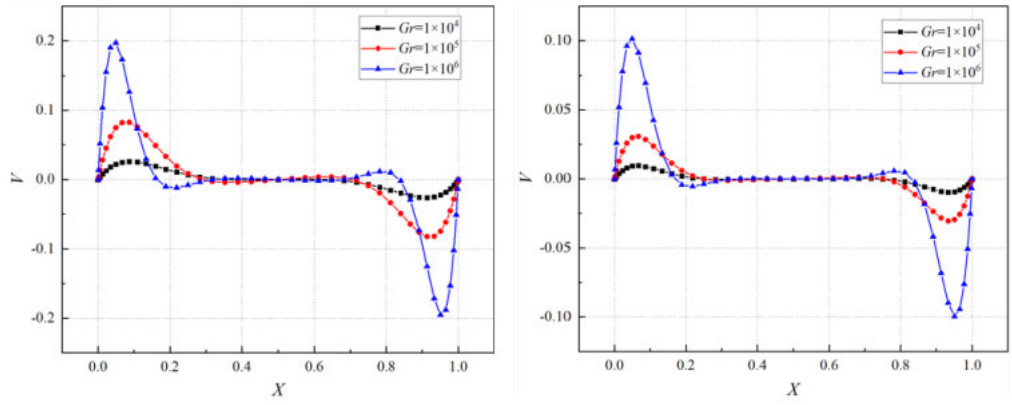

(c) *Ha*=50 (c) *Ha*=100

Fig. 13. The distribution of velocity *V* alone the line (*X*, 0.5, 0.5) for (a) *Ha*=0, (b) *Ha*=10, (c) *Ha*=50, and (d) *Ha*=100.

4.2 Effects of Hartmann number on natural convection

Using the same method as in section 4.1, we next investigate the effects of the magnetic field applied along the *Y* direction on flow and heat transfer at $Gr=1\times10^5$. Fig. 14 illustrates that increasing the Hartmann number results in isothermal surfaces that are approximately parallel to the *Y* direction, particularly for the central part of the cubic cavity. The temperature difference along the *Y* direction decreases.

Fig. 15 demonstrates that at the plane Z=0.5, the isotherms become approximately parallel to the isothermal walls as the Hartmann number increases. The magnetic field significantly restricts fluid flow along the X direction, and the boundary layers near the horizontal walls gradually disappears, while the boundary layers of the isothermal walls become thicker. These changes indicate that the heat transfer mode changes from convection to conduction, and the flow field structure in Fig. 16 changes to some extent.

Since the direction of the applied magnetic field is parallel to the Y-axis, the direction of the Lorentz force is perpendicular to the magnetic field direction, thus affecting the flow fields most significantly at the Y=0.5 plane. According to Fig. 17, as the Hartmann number increases, the thermal boundary layers expand towards the center. As shown in Fig. 18 (a) and Fig. 18 (b), when the Hartmann number increases from 10 to 50, the streamlines undergo significant changes. As Hartmann number continues to increase to 100, the changes become less pronounced.

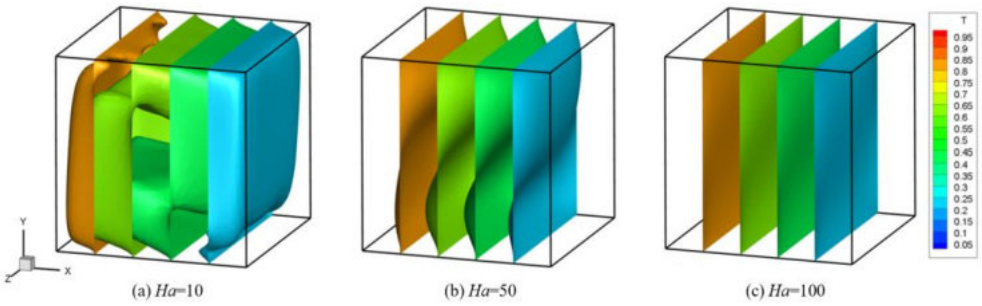

Fig. 14. The distribution of three-dimensional temperature isosurfaces at Gr=1×10^5 for (a) Ha=10, (b) Ha=50 and (c) Ha=100.

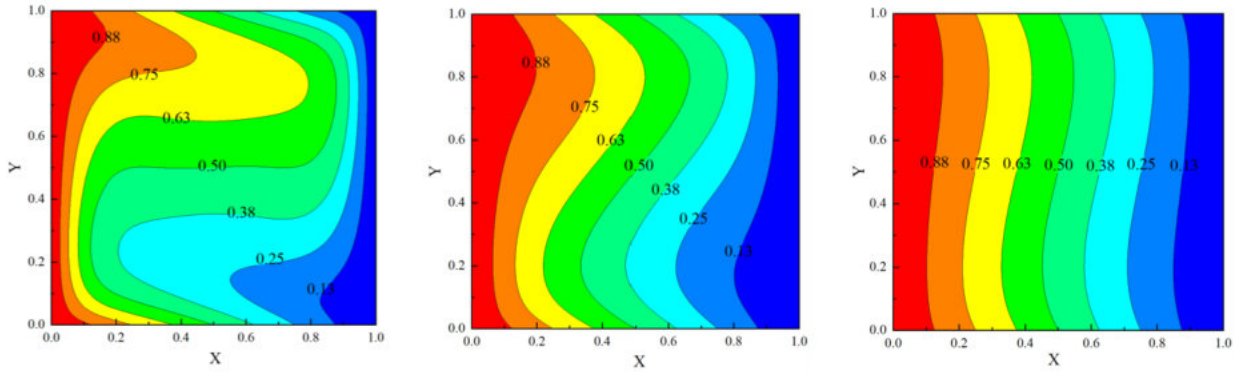

Fig. 15 The distribution of temperature on the plane Z=0.5 at Gr=1×10^5 for (a) Ha=10, (b) Ha=50 and (c) Ha=100.

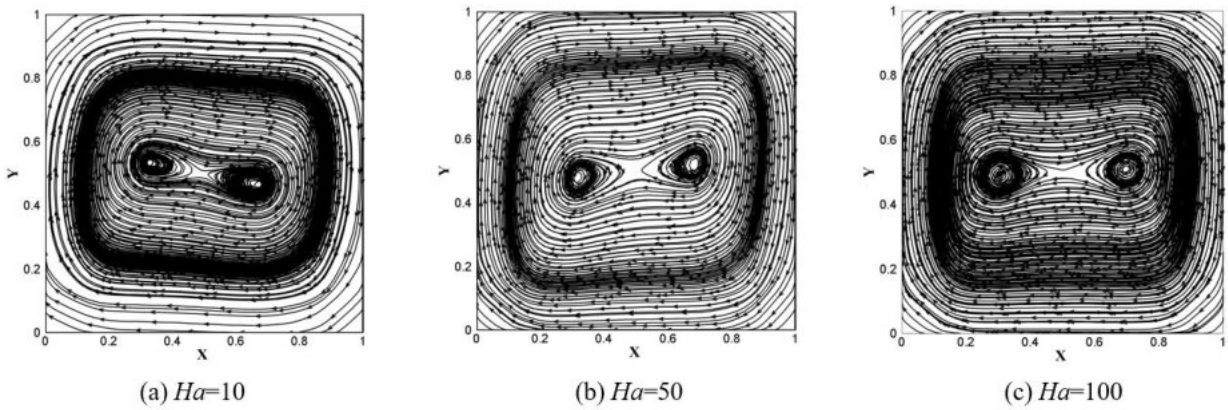

Fig. 16. The distribution of streamline on the plane Z=0.5 at Gr=1×10^5 for (a) Ha=10, (b) Ha=50 and (c) Ha=100.

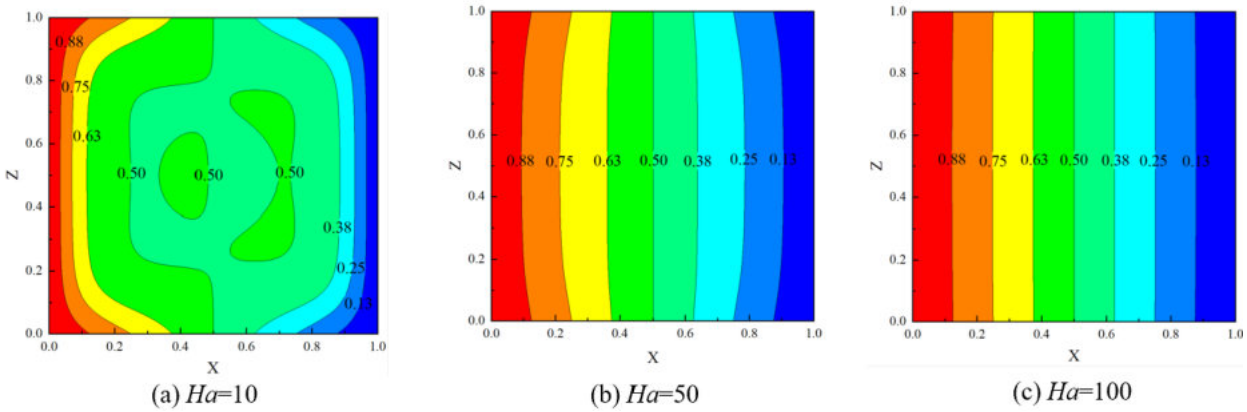

(a) Ha=10 (b) Ha=50 (c) Ha=100

Fig. 17 The distribution of temperature on the plane Y=0.5 at Gr=1×10^5 for (a) Ha=10, (b) Ha=50 and (c) Ha=100.

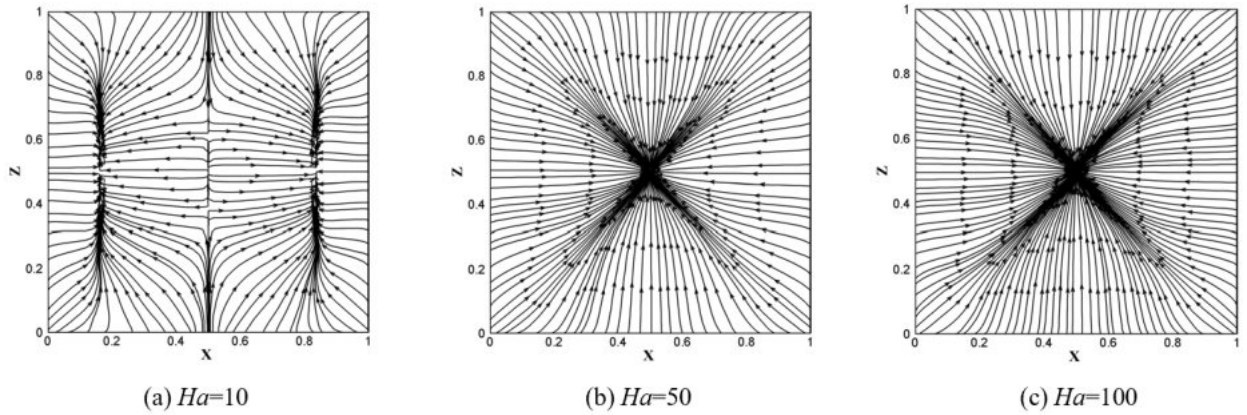

(a) Ha=10 (b) Ha=50 (c) Ha=100

Fig. 18. The distribution of streamline on the plane Y=0.5 at Gr=1×10^5 for (a) Ha=10, (b) Ha=50 and (c) Ha=100.

From Fig. 19, it can be observed that at the plane X=0.5 the increase of Hartmann number results in a decrease of the maximum temperature difference between the upper and lower parts of the cube. The streamline in Fig. 20 has also undergone significant changes.

Fig. 21 shows that when the Hartmann number increases from 0 to 100, the average Nusselt number of the hot wall decreases by 26.8%, 63.3%, and 64.9% for Gr=10^4, 10^5, and 10^6, respectively. Therefore, the magnetic field more obviously affects heat transfer under large Grashof numbers.

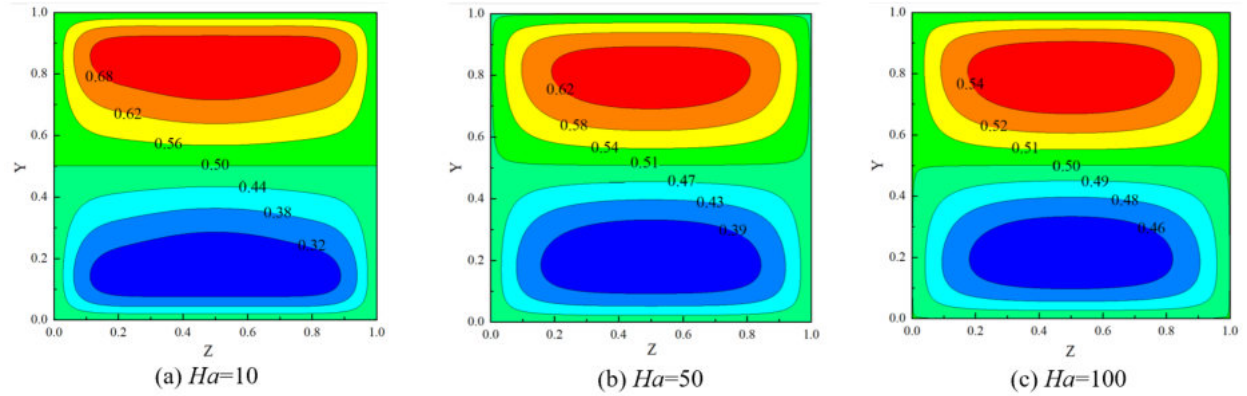

(a) Ha=10 (b) Ha=50 (c) Ha=100

Fig. 19 The distribution of temperature on the plane X=0.5 at Gr=1×10^5 for (a) Ha=10, (b)

***Ha*=50 and (c) *Ha*=100.**

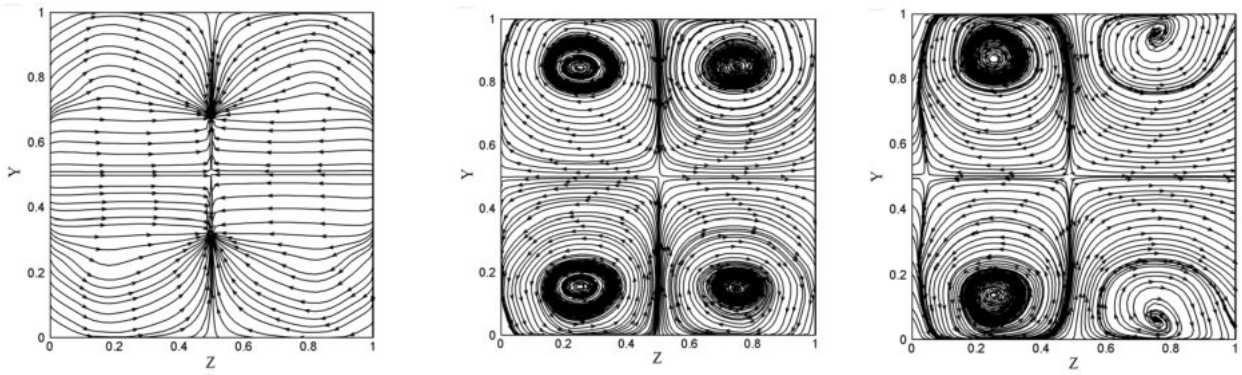

(a) *Ha*=10 (b) *Ha*=50 (c) *Ha*=100

Fig. 20. The distribution of streamline on the plane *X*=0.5 at *Gr*=1×10^5 for (a) *Ha*=10, (b) *Ha*=50 and (c) *Ha*=100.

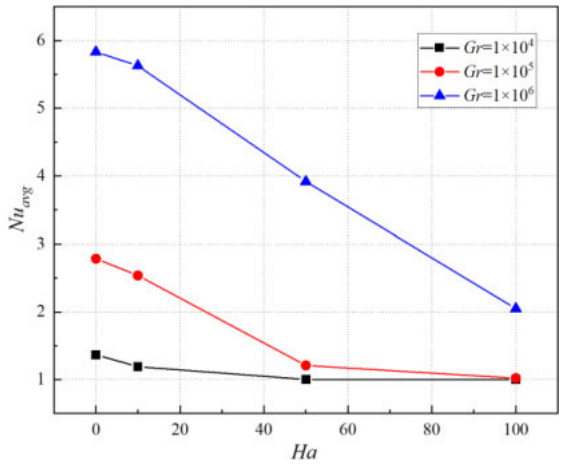

Fig. 21 The distribution of average Nusselt number with Hartmann numbers for different Grashof numbers.

Fig. 22 shows that as Hartmann number increases from 0 to 50, the local Nusselt number decreases significantly. When Grashof increases to 1×10^6, the magnetic field effects are not obvious, and the local Nusselt number is approximately equal to that under no magnetic field (*Ha*=0) at a relatively small Hartmann number (*Ha*=10). The positions corresponding to the maxima of the local Nusselt number remain nearly unchanged. For both smaller Grashof (*Gr*=1 × 10^4) and larger Hartmann number (*Ha*=100), the local Nusselt number is approximately equal to 1.

Fig. 23 reveals that an increase in the Hartmann number leads to a decrease in the velocity *V* along the *X* direction, and most of the regional flow in the square cavity is suppressed. The velocity and the structure of the flow field are more significantly affected by the Hartmann number for smaller Grashof numbers.

To better understand the influence of the magnetic field on the transverse velocity (*W*), we examine the maximum velocity value in the *Z* direction under *Ha*=0, 10, 30, 40, 50, 60, 80, and 100. Fig. 24 demonstrates that the velocity decreases significantly as the Hartmann number increases from 0 to 50, but the velocity changes little as the Hartmann number increases from 50 to 100.

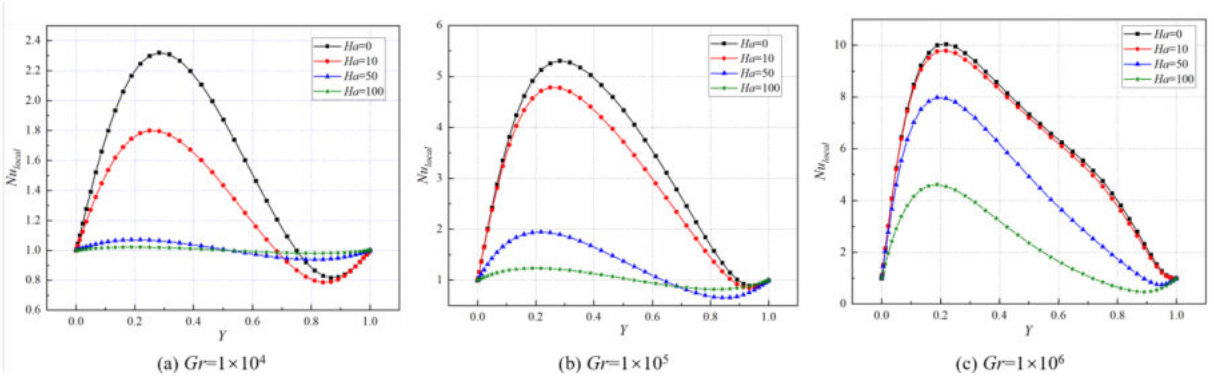

Fig. 22 The distribution of local Nusselt number alone the line (0, *Y*, 0.5) for (a) *Gr*= 1×10^4, (b) *Gr*=1×10^5 and (c) *Gr*=1×10^6.

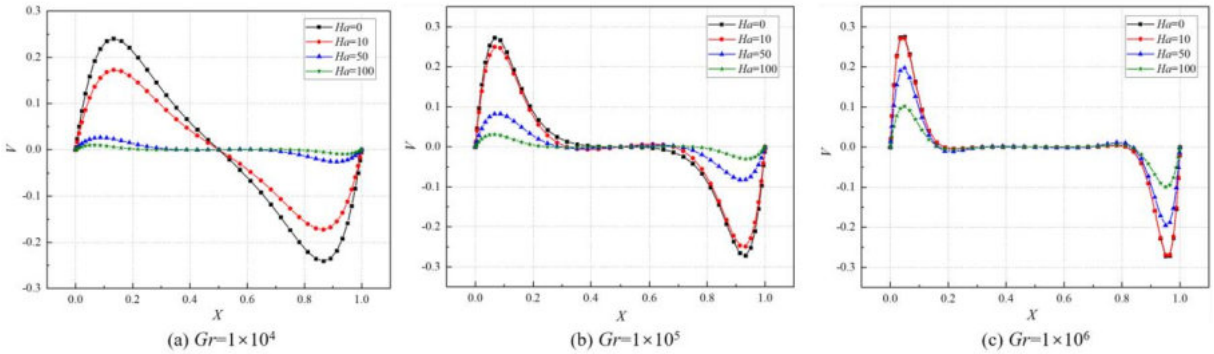

Fig. 23 The distribution of velocity *V* alone the line (*X*, 0.5, 0.5) for (a) *Gr*= 1×10^4, (b) *Gr*=1×10^5 and (c) *Gr*=1×10^6.

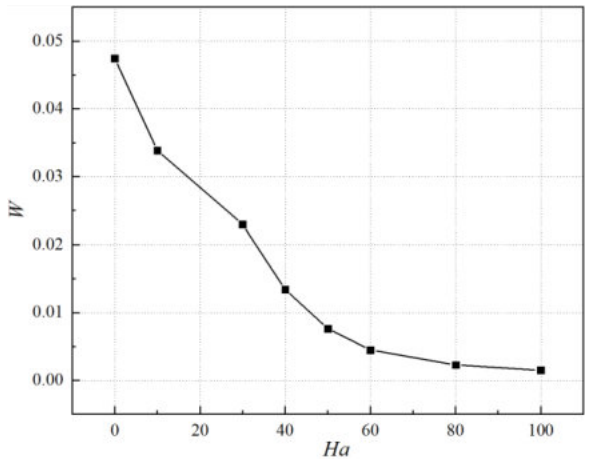

Fig. 24 The distribution of the maximum velocity (*W*) with Hartmann numbers at *Gr*=1×10^5.

4.3 The effects of magnetic field directions on natural convection

Later, we analyze the difference in the effects of magnetic field directions (B_X, B_Y) on heat transfer. Fig. 25 shows that the corresponding local Nusselt number of B_X is lower than that of B_Y at the height of 0-0.6, and higher than that of B_Y at 0.6-1.

Table 2 demonstrates that the averaged Nusselt number of the hot wall corresponding to B_Y is higher than that of B_X under any working condition. The difference becomes more apparent as

the Grashof number increases. Thus, we conclude that B_X has greater inhibitory effects on heat transfer than B_Y.

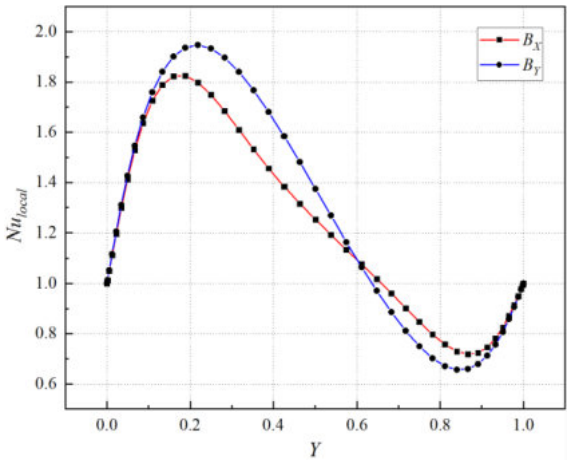

Fig. 25 The distribution of local Nusselt number alone the line (0, *Y*, 0.5) under the field of B_X and B_Y when $Gr=1\times10^5$.

Table 2 The averaged Nusselt number on the hot wall under different magnetic field directions.

Gr	*Ha*	Nu_{avg}	
		B_Y	B_X
10^4	0	1.367	1.367
	50	1.003	1.0025
10^5	0	2.785	2.785
	50	1.209	1.175
	100	1.021	1.013
10^6	0	5.831	5.831
	50	3.918	3.258
	100	2.049	1.638

5. Conclusion

In this paper, the MHD convection is investigated in a three-dimensional rectangular cavity filled with a conductive fluid. One pair of walls is maintained at a constant temperature and the others are thermally conducting. The flow and heat transfer equations are solved directly using the high-precision SCM-ACM, and the effects of magnetic field strength, directions, and Grashof numbers on the temperature and flow fields are analyzed. Based on the analysis, the following conclusions are drawn.

(1) For the temperature field, as the Grashof number increases, a stable thermal stratification forms at the center of the cubic cavity, and thermal boundary layers form near the horizontal walls. The increase in Grashof number enhances the heat transfer rate and increases the temperature difference between the upper hot fluid and the lower cold fluid in the cavity. The Hartmann number stabilizes the flow and weakens the heat transfer. The magnetic effects become more significant at higher Grashof numbers.

(2) For the flow field, the increase in Grashof number enhances the convective strength near the wall, resulting in the formation of more vortices inside the square cavity. Under the combined action of centrifugal force and inertial force, these vortices move towards the

corners. When the Hartmann number increases from 0 to 50, significant changes occur in the flow and temperature fields, but further increasing the Hartmann number has less influence. When $Ha > 60$, the velocity in the third direction approaches zero, simplifying the three-dimensional flow into two-dimensional flow.

(3) By comparing the heat transfer rates, we conclude that the magnetic field parallel to the temperature gradient (B_X) has a higher inhibiting effect on heat transfer compared to the magnetic field perpendicular to the temperature gradient (B_Y.)

References

[1] Kabeel, A. E., El-Said, E. M. and Dafea, S. A. (2015) A review of magnetic field effects on flow and heat transfer in liquids: Present status and future potential for studies and applications, *Renewable and Sustainable Energy Reviews* **45**, 830–837.

[2] Davidson, P. A. and Elena, V. B. (2002) An Introduction to Magnetohydrodynamics, *American Journal of Physics* **70**, 781.

[3] Kolsi, L., Oztop, H. F., Alghamdi, A., Abu-Hamdeh, N., Borjini, M. N. and Aissia, H. B. (2016) A computational work on a three dimensional analysis of natural convection and entropy generation in nanofluid filled enclosures with triangular solid insert at the corners, *Journal of Molecular Liquids* **218**, 260–274.

[4] Ismael, M. A., Armaghani, T. and Chamkha, A. J. (2016) Conjugate heat transfer and entropy generation in a cavity filled with a nanofluid-saturated porous media and heated by a triangular solid, *Journal of the Taiwan Institute of Chemical Engineers* **59**, 138–151.

[5] Selimefendigil, F. and Öztop, H. F. (2015) Natural convection and entropy generation of nanofluid filled cavity having different shaped obstacles under the influence of magnetic field and internal heat generation, *Journal of the Taiwan Institute of Chemical Engineers* **56**, 42–56.

[6] Garoosi, F., Hoseininejad, F. and Rashidi, M. M. (2016) Numerical study of natural convection heat transfer in a heat exchanger filled with nanofluids, *Energy* **109**, 664–678.

[7] Spizzichino, A., Zemach, E. and Feldman, Y. (2019) Oscillatory instability of a 3D natural convection flow around a tandem of cold and hot vertically aligned cylinders placed inside a cold cubic enclosure, *International Journal of Heat and Mass Transfer* **141**, 327-345.

[8] Bondareva, N. S. and Sheremet, M. A. (2016) Effect of inclined magnetic field on natural convection melting in a square cavity with a local heat source, *Journal of Magnetism and Magnetic Materials* **419**, 476–484.

[9] Saleh, H. and Hashim, I. (2016) Magnetohydrodynamic natural convection in a rotating enclosure, *Advances in Applied Mathematics and Mechanics* **8**, 279–292.

[10] Rudraiah, N., Barron, R. M., Venkatachalappa, M. and Subbaraya, C. K. (1995) Effect of a magnetic field on free convection in a rectangular enclosure, *International Journal of Engineering Science* **33**, 1075–1084.

[11] Sivasankaran, S. and Ho, C. J. (2008) Effect of temperature dependent properties on MHD convection of water near its density maximum in a square cavity, *International Journal of Thermal Sciences* **47**, 1184–1194.

[12] Sajjadi, H., Delouei, A. A., Atashafrooz, M. and Sheikholeslami, M. (2018) Double MRT Lattice Boltzmann simulation of 3-D MHD natural convection in a cubic cavity with sinusoidal temperature distribution utilizing nanofluid, I*nternational Journal of Heat and Mass Transfer* **126**, 489–503.

[13] Sajjadi, H., Delouei, A. A., Sheikholeslami, M., Atashafrooz, M. and Succi, S. (2019) Simulation of three dimensional MHD natural convection using double MRT Lattice Boltzmann method, *Physica A: Statistical Mechanics and Its Applications* **515**, 474–496.

[14] Zhou, W., Yan, Y., Xie, Y. and Liu, B. (2017) Three dimensional lattice Boltzmann simulation for mixed convection of nanofluids in the presence of magnetic field, *International Communications in Heat and Mass Transfer* **80,** 1–9.

[15] Sheikholeslami, M. and Ellahi, R. (2015) Three dimensional mesoscopic simulation of magnetic field effect on natural convection of nanofluid, *International Journal of Heat and Mass Transfer* **89**, 799–808.

[16] Gelfgat, A. Y. and Zikanov, O. (2018) Computational modeling of magnetoconvection: effects of discretization method, grid refinement and grid stretching, *Computers & Fluids* **175**, 66–82.

[17] Bouchta, S., Feddaoui, M. B. and Dayf, A. (2021) Numerical simulation of free convection in a partially heated three-dimensional enclosure filled with ionanofluid ([C4mim][NTf2]-Cu), *Mathematical Problems in Engineering* **2021**, 1–11.

[18] Okada, K. and Ozoe, H. (1992) Experimental heat transfer rates of natural convection of molten gallium suppressed under an external magnetic Field in either the X, Y, or Z Direction, *Journal of Heat Transfer* **114**, 107–114.

[19] Ozoe, H. and Okada, K. (1989) The effect of the direction of the external magnetic field on the three-dimensional natural convection in a cubical enclosure, *International Journal of Heat and Mass Transfer* **32**,1939–1954.
[20] Zhang, J. K., Cui, M., Li, B. W. and Sun, Y. S. (2020), Performance of combined spectral collocation method and artificial compressibility method for 3D incompressible fluid flow and heat transfer, *International Journal of Numerical Methods for Heat & Fluid Flow* **30**, 5037–5062.
[21] Kajzer, A. and Pozorski, J. (2018) Application of the entropically damped artificial compressibility model to direct numerical simulation of turbulent channel flow, *Computers & Mathematics with Applications* **76**, 997–1013.
[22] Ramachandran, P. and Puri, K. (2019) Entropically damped artificial compressibility for SPH, *Computers & Fluids* **179**, 579–594.
[23] Bogaers, A. E., Kok, S., Reddy, B. D. and Franz, T. (2015) Extending the robustness and efficiency of artificial compressibility for partitioned fluid–structure interactions, *Computer Methods in Applied Mechanics and Engineering* **283**, 1278–1295.
[24] Wang, W., Li, B. W., Varghese, P. L., Leng, X. Y. and Tian, X. Y. (2018) Numerical analysis of three-dimensional MHD natural convection flow in a short horizontal cylindrical annulus, *International Communications in Heat and Mass Transfer* **98,** 273–285.
[25] Zhang, J. K., Dong, H., Zhou, E. Z., Li, B. W. and Tian, X. Y. (2017) A combined method for solving 2D incompressible flow and heat transfer by spectral collocation method and artificial compressibility method, *International Journal of Heat and Mass Transfer* **112**, 289–299.
[26] Chattopadhyay, G., Ranganathan, U. and Millet, S. (2019) Instabilities in viscosity-stratified two-fluid channel flow over an anisotropic-inhomogeneous porous bottom, *Physics of Fluids* **31**, 012103.
[27] Merrill, B. E. and Peet, Y. T. (2019) Moving overlapping grid methodology of spectral accuracy for incompressible flow solutions around rigid bodies in motion, *Journal of Computational Physics* **390**, 121–151.
[28] Raj, R. and Guha, A. (2019) On Bragg resonances and wave triad interactions in two-layered shear flows, *Journal of Fluid Mechanics* **867**, 482–515.
[29] Pourjafar, M., Hejri, A., Bazargan, S. and Sadeghy, K. (2018) On the use of a fluid's elasticity for deliberate rise of Taylor cells in a rotating micro-filter separator, *Physics of Fluids* **30**, 114106.
[30] Fusegi, T., Hyun, J. M., Kuwahara, K. and Farouk, B. (1991) A numerical study of three-dimensional natural convection in a differentially heated cubical enclosure, *International Journal of Heat and Mass Transfer* **34**, 1543-1557.
[31] Tric, E., Labrosse, G. and Betrouni, M. (2000) A first incursion into the 3D structure of natural convection of air in a differentially heated cubic cavity, from accurate numerical solutions, *International Journal of Heat and Mass Transfer* **43**, 4043-4056.
[32] Wakashima, S. and Saitoh, T. S. (2004) Benchmark solutions for natural convection in a cubic cavity using the high-order time–space method, *International Journal of Heat and Mass Transfer* **47**, 853–864.
[33] Luo, X. H., Li, B. W. and Hu, Z. M. (2016) Effects of thermal radiation on MHD flow and heat transfer in a cubic cavity, *International Journal of Heat and Mass Transfer* **92**, 449–466.
[34] Singh, R. J. and Gohil, T. B. (2019) The numerical analysis on the development of Lorentz force and its directional effect on the suppression of buoyancy-driven flow and heat transfer using OpenFOAM. *Computers & Fluids* **179**, 476-489.